electronics

MDPI

Article

Phase Shift Optimization Algorithm for Achievable Rate Maximization in Reconfigurable Intelligent Surface-Assisted THz Communications

João Praia [1,2,*], João Pedro Pavia [1,2], Nuno Souto [1,2] and Marco Ribeiro [1,2]

[1] Department of Information Science and Technology, ISCTE-University Institute of Lisbon, 1649-026 Lisboa, Portugal; Joao_Pedro_Pavia@iscte-iul.pt (J.P.P.); Nuno.Souto@iscte-iul.pt (N.S.); Marco.Ribeiro@iscte-iul.pt (M.R.)
[2] Instituto de Telecomunicações, 1049-001 Lisboa, Portugal
* Correspondence: Joao_Praia@iscte-iul.pt

Abstract: Terahertz (THz) band communications are considered a crucial technology to support future applications, such as ultra-high bit rate wireless local area networks, in the next generation of wireless communication systems. In this work, we consider an ultra-massive multiple-input multiple-output (UM-MIMO) THz communication system operating in a typical indoor scenario where the direct link between the transmitter and receiver is obstructed due to surrounding obstacles. To help establish communication, we assume the aid of a nearby reconfigurable intelligent surface (RIS) whose phase shifts can be adjusted. To configure the individual phase shifts of the RIS elements, we formulate the problem as a constrained achievable rate maximization. Due to the typical large dimensions of this optimization problem, we apply the accelerated proximal gradient (APG) method, which results in a low complexity algorithm that copes with the non-convex phase shift constraint through simple element-wise normalization. Our numerical results demonstrate the effectiveness of the proposed algorithm even when considering realistic discrete phase shifts' quantization and imperfect channel knowledge. Furthermore, comparison against existing alternatives reveals improvements between 30% and 120% in terms of range, for a reference rate of 100 Gbps when using the proposed approach with only 81 RIS elements.

Keywords: terahertz (THz) communications; reconfigurable intelligent surface (RIS); achievable rate; ultra-massive multiple-input multiple-out (UM-MIMO)

Citation: Praia, J.; Pavia, J.P.; Souto, N.; Ribeiro, M. Phase Shift Optimization Algorithm for Achievable Rate Maximization in Reconfigurable Intelligent Surface-Assisted THz Communications. *Electronics* **2022**, *11*, 18. https://doi.org/10.3390/electronics11010018

Academic Editor: Tadeusz A. Wysocki

Received: 11 November 2021
Accepted: 18 December 2021
Published: 22 December 2021

1. Introduction

With the commercial deployment of the fifth generation of wireless communications (5G), academic and industry efforts are now focused on the sixth generation of wireless communications (6G) [1–3]. In 6G networks, substantial coverage and data rate improvements are expected, enabling denser networks and global connectivity. Therefore, new emerging technologies are needed to meet the future demands of 6G wireless systems, with THz communications being one of the most promising research fields on the subject. It is noted, however, that some of the current research areas for the development of 5G devices are fundamental in the study of THz waves and 6G. Such is the case of metamaterials and photonic band gaps (MTM–PBG), which have recently been used to demonstrate effective mutual coupling reduction techniques for synthetic-aperture radar and MIMO antenna systems that require high transmit/receive isolation [4,5]. These simple techniques, which find applications in existing array antennas, can be very promising in THz too.

Unlike mmWave communications, the THz band can enable low latency, high reliability, and terabit/second data rates without additional techniques to improve spectral efficiency [6]. However, adopting the Terahertz band (0.1–10 THz) in wireless communication environments introduces several challenges [7]. In fact, the high propagation losses in the THz band and the existing power constraints significantly limit the communication

distance [8]. Furthermore, obstacles in the wireless communication environment can easily block THz signals due to their poor diffraction and scattering capabilities [9].

In order to overcome these problems, work on smart communication environments for the THz band has been attracting significant attention recently, which relies on the emerging concept of Reconfigurable Intelligent Surfaces (RIS) [10–12]. Specifically, RIS are flat electromagnetic (EM) material surfaces composed of an array of dispersive elements. Each element can induce an amplitude and/or phase shift to the incident signal to enhance the received signal power and create a desirable multipath effect without the need for complex coding and decoding schemes or without additional frequency radio (FR) operations. Considering that it is expensive to implement simultaneous independent control of reflection amplitude and phase shift, each RIS element is usually designed to maximize signal reflection only [10,13]. The design and prototyping processes of this type of reflective surface are currently considered significant issues, which are especially challenging from the point of view of energy consumption and hardware costs [14].

When implemented in a wireless communications environment, RIS enables extended coverage, low power consumption, and more secure transmissions [15]. Thus, the integration of RIS in THz communications is considered a promising solution. In [16,17], potential applications of RIS to overcome the strong propagation attenuations at THz frequencies are presented. Due to the envisioned low complexity of RIS, these devices may be conveniently installed in ceilings, walls, furniture, building facades, and other reflecting objects, improving significantly the coverage of THz communications. Therefore, RIS are considered fundamental building blocks for ultra-high bitrate wireless local area networks (WLAN) that can support demanding applications among mobile or static users, such as virtual/augmented reality or holographic projection [18], in indoor and outdoor scenarios. Other relevant applications that are foreseen to benefit from RIS-aided THz communications are ultra-high speed indoor ad hoc connections between devices, for example between a laptop and a camera, and the deployment of ultra-high data rate indoor and outdoor nano-cells in cellular networks [19,20]. In [11], the authors present some THz-RIS communication scenarios and address the joint formation of active and passive beams as a strategy to improve energy efficiency (EE) and provide virtual line-of-sight (LoS) paths to reduce the blocking probability.

RIS are key devices for future communications in higher frequency bands, but the reality is that they are already just as important for lower frequency bands. Recently, several RIS-aided wireless communication systems have emerged as solutions to improve wireless communications at sub-6 GHz and mmWave bands [21]. When concerning indoor environments, the achievable rate of the system can be optimized based on a small number of RIS elements, since they can be enough to allow the indirect connection to achieve a higher rate than the direct connection, as referred to in [22]. Another example is a practical RIS network designed in [23], which considers users' position by using stochastic geometry (SG). The authors prove that by increasing the number of antennas in the base station (BS) or the RIS elements, spectral efficiency (SE) and EE can be improved. Moreover, the fading distribution among the RIS and users has only a slight impact on the network performance. The study in [24] focuses on maximizing the achievable ergodic rate of the system, where the design of the diagonal phase-shifting matrix is obtained by using the projected gradient ascent method. The results show that the proposed algorithm can significantly enhance the RIS-assisted MIMO system performance. Besides the schemes described above, recent progress in this field has resulted in several promising RIS-based solutions, which are detailed in Table 1. It can be noticed from the table that many of the schemes are aimed at multi-input single-output (MISO) IRS-assisted systems operating in lower frequency bands.

Table 1. Relevant works on the topic from the literature.

Reference	System Model	Main Aspects	Issues
[25]	RIS-aided multiuser MISO communication system	Proposed an alternating optimization (AO) algorithm for multiuser RIS-aided MIMO that iteratively optimizes the RIS phase shifts and the transmit beamforming vector. The coverage and achievable rate performance are significantly improved when compared to conventional systems without RIS.	To achieve the desired convergence, the AO algorithm requires a large number of iterations, especially when the number of RIS elements is large. Furthermore, the algorithm was designed assuming lower band single antenna users, which, combined with a computational complexity that is strongly dependent on the transmitter array size, makes it difficult to extend to UM-MIMO THz systems.
[26]	RIS-aided multiuser MISO communication system	Considered an RIS-based downlink multiuser multiantenna system with limited discrete phase shifts, operating in the absence of direct links between the BS and users. Proposed an iterative algorithm in which the transmitter digital beamforming subproblem is solved through zero-forcing with power allocation and the RIS-based analog beamforming is solved by the outer approximation method. It was shown that good sum-rate performances can be achieved with a reasonable sized RIS and a small number of discrete phase shifts.	It assumes single antenna users and the computational complexity can grow prohibitively high for large arrays, which compromises its potential application in UM-MIMO THz systems.
[22]	RIS-aided MIMO communication system	Derived an iterative algorithm for solving the joint optimization problem of the covariance matrix of the transmitted signal and the RIS elements. The resulting algorithm was shown to achieve similar achievable rate gains to the method from [25] in single-user scenarios but requires fewer iterations.	It was designed to target lower frequency bands, as well as having a computational complexity that is strongly dependent on the number of transmitter antennas. Therefore, applying this approach with the large array of settings envisioned for UM-MIMO THz systems can be very challenging.
[27]	RIS-aided MIMO THz system	Developed an adaptive gradient descent (A-GD) algorithm for single-user RIS-aided MIMO THz systems. The proposed A-GD algorithm improves the achievable rate performance when compared with other alternative algorithms. The A-GD algorithm considers discrete phase shifts through a final mapping step.	The A-GD algorithm can achieve large gains over an RIS with random phase, shifts but the computational complexity becomes very high when working with large antenna arrays and RISs with a large number of elements.
Our approach	RIS-aided MIMO THz system	Applied the APG method to a phase shift constrained maximum achievable rate problem. A low complexity algorithm resorting to simple element-wise normalization was derived that can cope with the large problem settings of RIS-aided UM-MIMO systems in the THz band. The proposed algorithm can handle discrete phase shifters with amplitude loss. Numerical evaluation shows that the proposed scheme can achieve competitive performance gains when compared against state-of-the-art solutions, as in [27].	The approach was designed for single-user scenarios. As future work, it may be extended to multiuser cases.

Another potential solution to effectively overcome the severe path loss in the THz band corresponds to ultra-massive MIMO (UM-MIMO) schemes based on ultra-dense arrays of sub-millimeter wavelength antennas, which has been proposed in [17]. Relying on this UM-MIMO approach, some recent solutions have already been described in the literature [28,29]. To make UM-MIMO realizable, several different fabrications techniques for THz band antennas are being explored by researchers, with some of them resorting to new materials [30]. One of the most promising approaches lies on graphene-based large-scale antenna arrays [31]. However, most works regarding graphene and other new materials-based THz antenna arrays are in the stage of theoretical design and analysis [31–34], still lacking experimental exploration [30]. Therefore, the establishment

of a complete array architecture for true THz frequencies with dynamic beamforming that can be used in UM-MIMO is still difficult to accomplish. However, a few works focusing on theoretical and numerical performance analysis for RIS-aided UM-MIMO schemes have started to appear [6,27,30,35]. Apart from the research works mentioned above, the achievable rate and performance analyses for RIS-assisted UM-MIMO communication systems are still treated as an open problem. It is important to note that UM-MIMO relies on the idea of adopting large-scale integrated phased arrays with a very small footprint in order to overcome the high path losses at the THz band. An important challenge regarding these very large arrays is how to characterize the interaction and coupling effects among adjacent elements [36]. Mutual coupling was studied in [37] for densely packed metamaterial-based antennas operating at THz frequencies, with the authors incorporating a resonator-based metasurface in order to mitigate its effect. Graphene-based large-scale antenna arrays are considered a promising alternative to traditional antennas in the THz band. Regarding graphene-based THz antenna arrays, the mutual coupling effects were studied in [38,39]. In [38], the authors showed that in graphene-based plasmonic nano-antenna arrays, the effect of mutual coupling between antennas becomes negligible at separation distances much less than the free space wavelength. In [39], the authors showed that by adopting a graphene-based frequency selective surface (FSS) structure, the mutual coupling effects become negligible even in the presence of a very large number of closely integrated elements.

In this paper, we study the transmission design for a THz UM-MIMO system operating in an indoor scenario, where a BS transmits to a user with the aid of a passive RIS. The aim of this work is to maximize the achievable rate over the distance between the BS and the user. To accomplish this, and at the same time cope with the large dimensions of RIS-aided UM-MIMO systems, we formulate the RIS design (i.e., phase shifts) as a non-convex optimization problem and derive an Accelerated Projected Gradient (APG)-based algorithm to solve it. To facilitate a direct comparison between the present work and existing state-of-the-art approaches, we include some of the most relevant aspects of the proposed scheme in Table 1. Since the implementation of an experimental RIS-assisted UM-MIMO testbed in the THz band is still a challenging task due to current limitations of practical reconfigurable large-scale THz antenna arrays, in this paper we adopt the approach followed by most works in RIS-assisted UM-MIMO and evaluate the proposed algorithm through numerical simulations. To accomplish the numerical evaluation, we adopt a typical THz channel model that captures most of the relevant effects at this band. Performance results demonstrate the effectiveness of the proposed algorithm in helping to overcome the distance limitation in the THz band, with the achievable rate being significantly improved by increasing the number of RIS elements. Furthermore, we consider the impact of phase quantization in the RIS elements and also of imperfect channel knowledge. This paper is organized as follows: section II presents the model for the RIS-assisted UM-MIMO system. Section III derives the phase-shifting matrix design algorithm followed by the numerical results in section IV. Finally, the conclusions are outlined in section V.

Notation: Bold lower and upper-case letters represent vectors and matrices, respectively. $\mathbb{C}^{a\times b}$ denotes the space of complex matrices of dimensions $a \times b$, $(\cdot)^{\mathrm{H}}$ denotes the conjugate transpose of a matrix/vector, *diag* (**a**) is a diagonal matrix with elements of **a** on its diagonal, and $\mathbf{I}_n$ is the $n \times n$ identity matrix.

2. System Model

Let us consider the UM-MIMO communication system illustrated in Figure 1, which can represent an envisioned THz band WLAN application scenario where a base station with an array of N_{tx} antennas transmits to a user with N_{rx} antennas. Assuming an indoor environment where surrounding obstacles can easily obstruct a direct link, then the communication link can be established with the aid of an RIS panel with N_{RIS} elements deployed, for example, on a nearby wall. Note that without loss of generalization, the figure is assuming a 2D deployment (x,y coordinate system) to simplify the explanations.

Each transmission comprises N_s simultaneous data streams, which are represented as $\mathbf{s} = [s_1 \dots s_{N_s}]^T$, with $s_i \in \mathbb{C}$ corresponding to an amplitude and phase modulated symbol and $\mathrm{E}\left[\|\mathbf{s}\|^2\right] = N_s$. We consider a typical discrete-time complex baseband representation for the received signal, which is a vector-based representation that is often adopted in signal processing works for MIMO communications in the THz band [6,27,40]. It allows modeling the effect on the amplitude and phase of the information symbols after passing through all possible transmit–RIS–receiver array links and after being processed by the precoder and combiner. Using this representation, the signal arriving at the user, can be expressed as

$$\mathbf{r} = \sqrt{\rho}\mathbf{W}^H\mathbf{H}^{D,RIS}\mathbf{\Phi}\mathbf{H}^{RIS,S}\mathbf{F}\mathbf{s} + \mathbf{n} \tag{1}$$

where $\sqrt{\rho}$ denotes the power per stream, $\mathbf{F} \in \mathbb{C}^{N_{tx} \times N_s}$ is the base station precoder matrix, $\mathbf{W} \in \mathbb{C}^{N_{rx} \times N_s}$ is the user combining matrix, $\mathbf{n} \in \mathbb{C}^{N_{rx} \times 1}$ is the noise vector, which contains independent zero-mean circularly symmetric Gaussian samples with covariance $\sigma_n^2\mathbf{I}_{N_{rx}}$, $\mathbf{H}^{RIS,S} \in \mathbb{C}^{N_{ris} \times N_{tx}}$ is the channel matrix between the base station and the RIS, and $\mathbf{H}^{D,RIS} \in \mathbb{C}^{N_{rx} \times N_{ris}}$ is the channel matrix between the RIS and the user. Matrix $\mathbf{\Phi} \in \mathbb{C}^{N_{ris} \times N_{ris}}$ models the effect of the RIS panel, having a diagonal structure with $\mathbf{\Phi} = \mathrm{diag}(\boldsymbol{\varphi})$ where $\boldsymbol{\varphi} = \left[\varphi_1, \dots, \varphi_{N_{ris}}\right]^T$ and φ_m represents the phase shift of the m^{th} RIS element.

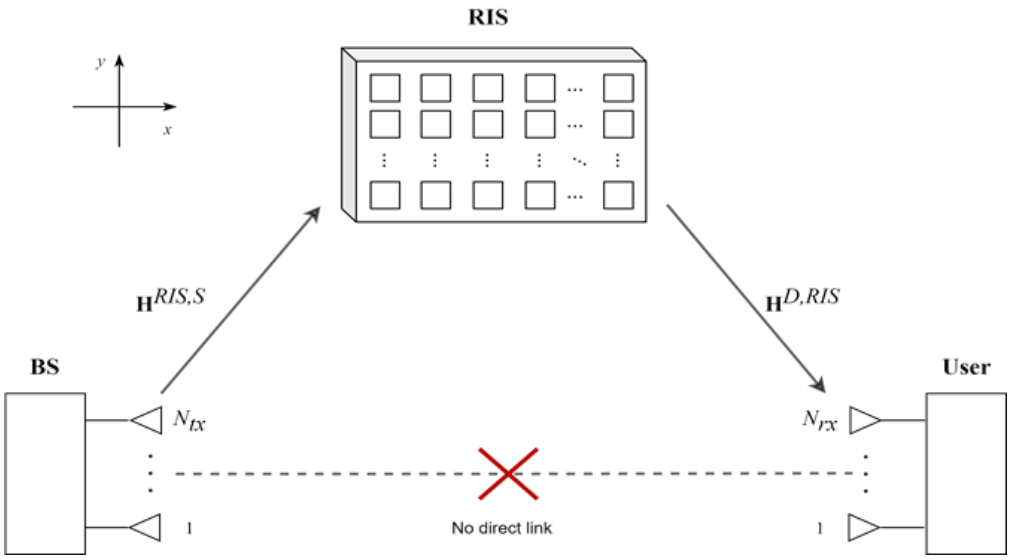

Figure 1. An RIS-assisted UM-MIMO system consisting of a BS, a user, and an RIS with N_{RIS} reflecting elements.

We consider a clustered geometric channel model [41], which is commonly adopted in THz literature [27]. Furthermore, we assume that the channels consist of a LoS component, denoted as $\mathbf{H}_{LOS}^{RIS,S}$, and N_{ray} Non-Line-of-Sight (NLoS) paths as in [27]. In this case we can write

$$\mathbf{H}^{RIS,S} = \mathbf{H}_{LOS}^{RIS,S} + \sqrt{\frac{\beta_{NLOS}^{RIS,S}}{K_{Rice}}} \sum_{l=1}^{N_{ray}} \alpha_l^{RIS,S} \mathbf{a}_{RIS}\left(\phi_l^{RIS \leftarrow S}, \theta_l^{RIS \leftarrow S}\right) \mathbf{a}_S\left(\phi_l^{S \rightarrow RIS}, \theta_l^{S \rightarrow RIS}\right)^H \tag{2}$$

for the channel between the base station and the RIS, where $\alpha_l^{RIS,S}$ is the complex gain of the lth NLOS ray (with $\sum_{l=1}^{N_{ray}} E\left[\left|\alpha_l^{RIS,S}\right|^2\right] = 1$) and $\beta_{NLOS}^{RIS,S}$ denotes the path loss of the NLoS channel. Assuming path lengths close to $d_{S \leftrightarrow RIS}$, this path loss can be approximated as

$$\beta_{NLOS}^{RIS,S} = \frac{G_{tx} A_{RIS}}{4\pi \left(d_{S \leftrightarrow RIS}\right)^2} e^{-k_{abs}(f) d_{S \leftrightarrow RIS}} \tag{3}$$

which allows us to use the Rice factor, K_{Rice}, to define the energy ratio between the LoS and NLoS components. Vectors $\mathbf{a}_S\left(\phi_l^{S\to RIS}, \theta_l^{S\to RIS}\right)$ and $\mathbf{a}_{RIS}\left(\phi_l^{RIS\leftarrow S}, \theta_l^{RIS\leftarrow S}\right)$ represent the transmit antenna array and RIS array responses at the $\left(\phi_l^{RIS\leftarrow S}, \theta_l^{RIS\leftarrow S}\right)$ and $\left(\phi_l^{S\to RIS}, \theta_l^{S\to RIS}\right)$ azimuth and elevation angles, respectively. Assuming the adoption of a uniform planar array (UPA) structure, the steering vectors for the transmitter are given by

$$\mathbf{a}_S\left(\phi_l^{S\to RIS}, \theta_l^{S\to RIS}\right) = \Big[1, \ldots, e^{j\frac{2\pi}{\lambda} d_S\left(p \sin\phi_l^{S\to RIS} \sin\theta_l^{S\to RIS} + q\cos\theta_l^{S\to RIS}\right)}, \ldots, e^{j\frac{2\pi}{\lambda} d_S\left((\sqrt{N_{tx}}-1)\sin\phi_l^{S\to RIS}\sin\theta_l^{S\to RIS} + (\sqrt{N_{tx}}-1)\cos\theta_l^{S\to RIS}\right)}\Big]^T \tag{4}$$

where $p, q = 0, \ldots, \sqrt{N_{tx}} - 1$ are the antenna indices, λ is the signal wavelength, and d_s is the inter-element spacing at the transmit array. The steering vectors for the RIS and receiver, $\mathbf{a}_{RIS}\left(\phi_l^{RIS\leftarrow S}, \theta_l^{RIS\leftarrow S}\right)$ and $\mathbf{a}_D\left(\phi_l^{D\leftarrow RIS}, \theta_l^{D\leftarrow RIS}\right)$, can be defined using a similar notation. Assuming a unit normalized power radiation pattern for the antennas and RIS elements along the directions of interest, the components of $\mathbf{H}_{LOS}^{RIS,S}$ can be written as [35,42]

$$\mathbf{H}_{LOS}^{RIS,S}(n,m) = \sqrt{\frac{G_{tx} A_{RIS}}{4\pi {d_{n,m}}^2} e^{-k_{abs}(f) d_{n,m}}} e^{-j2\pi d_{n,m}/\lambda} \tag{5}$$

where $d_{n,m}$ represents the distance between the mth transmit antenna element and the nth RIS element, G_{tx} is the transmit antenna gain, A_{RIS} is the RIS element area, and $k_{abs}(f)$ is the molecular absorption coefficient at frequency f.

Using a similar notation, we can write the channel between the RIS and the user as

$$\mathbf{H}^{D,RIS} = \mathbf{H}_{LOS}^{D,RIS} + \sqrt{\frac{\beta_{NLOS}^{RIS,S}}{K_{Rice}}} \sum_{l=1}^{N_{ray}} \alpha_l^{D,RIS} \mathbf{a}_D\left(\phi_l^{D\leftarrow RIS}, \theta_l^{D\leftarrow RIS}\right) \mathbf{a}_{RIS}\left(\phi_l^{RIS\to D}, \theta_l^{RIS\to D}\right)^H \tag{6}$$

It is important to note that the effect of mutual coupling can be included in the system model by multiplying the steering vectors by $N_{tx} \times N_{tx}$ ($N_{rx} \times N_{rx}$ in case of the receiver) mutual coupling matrices, $\mathbf{a}'_S\left(\phi_l^{S\to RIS}, \theta_l^{S\to RIS}\right) = \mathbf{C}_S \mathbf{a}_S\left(\phi_l^{S\to RIS}, \theta_l^{S\to RIS}\right)$ [6]. The coupling matrices reduce to the identity matrix when the effect can be neglected, which can be acceptable in graphene-based plasmonic nano-antenna arrays at THz frequencies for separation distances much less than the free space wavelength, as discussed in [38].

3. Phase-Shifting Matrix Optimization

3.1. Problem Formulation

After describing the system model and the channel model in the previous section, we can focus on the problem formulation by defining the combined channel matrix as

$$\mathbf{H}^{Total}(\boldsymbol{\varphi}) = \mathbf{H}^{D,RIS} \boldsymbol{\Phi} \mathbf{H}^{RIS,S} \tag{7}$$

with $\boldsymbol{\Phi} = \mathrm{diag}(\boldsymbol{\varphi})$. We can then rewrite the received signal (1) as

$$\mathbf{r} = \sqrt{\rho} \mathbf{W}^H \mathbf{H}^{Total}(\boldsymbol{\varphi}) \mathbf{F} \mathbf{s} + \mathbf{n} \tag{8}$$

To limit the implementation complexity, in this paper, we consider that the precoder is designed first with the RIS matrix being optimized based on this precoder. It should be noted that the proposed design can also be directly extended to an alternating optimization approach by subsequently recomputing the precoding matrix followed by another computation of the RIS matrix. While this can improve the performance, it also increases the complexity. Regarding the base station precoder, we consider the use of a singular value decomposition (SVD)-based design. In this case, we decompose $\mathbf{H}^{Total}(\boldsymbol{\varphi})$ into

$$\mathbf{H}^{Total}(\boldsymbol{\varphi}) = \mathbf{U} \boldsymbol{\Lambda} \mathbf{V}^H \tag{9}$$

where $\mathbf{U}$ is a unitary matrix $N_{rx} \times N_{rx}$, $\mathbf{\Lambda}$ is a diagonal matrix of dimension $N_{rx} \times N_{tx}$, and $\mathbf{V}$ is a unitary matrix $N_{tx} \times N_{tx}$. The precoder matrix is then simply set as $\mathbf{F} = \mathbf{V}[:, 1 : N_s]$. It is important to highlight that while we are assuming a fully digital precoder in this exposition, it is well-known that UM-MIMO operating in the THz bands must rely on hybrid implementations, where the signal processing is split into a reduced digital part and an analog part. However, the hybrid design can be easily obtained through direct approximation of the fully digital precoder matrix using the product of a smaller digital precoder matrix and an analog precoder matrix, as described in [43,44].

For the computation of the RIS matrix, we can maximize the maximum achievable rate of the system, which for a given precoder matrix $\mathbf{F}$ and assuming perfect channel knowledge can be written as

$$R = \log_2 \det\left(\mathbf{I}_{Ns} + \frac{\rho}{P_n}\mathbf{F}^H\mathbf{H}^{Total^H}(\boldsymbol{\varphi})\mathbf{H}^{Total}(\boldsymbol{\varphi})\mathbf{F}\right) \tag{10}$$

in bits/s/Hz, with P_n denoting the noise power (i.e., $P_n = \sigma_n^2$). The optimization problem can then be formulated as

$$\min_{\boldsymbol{\varphi}} -\ln \det\left(\mathbf{I}_{Ns} + \frac{\rho}{P_n}\mathbf{F}^H\mathbf{H}^{Total^H}(\boldsymbol{\varphi})\mathbf{H}^{Total}(\boldsymbol{\varphi})\mathbf{F}\right)$$
$$\text{subject to } |\boldsymbol{\varphi}| = a \tag{11}$$

Constraint $|\boldsymbol{\varphi}| = a$ is applied to each individual RIS element, with a denoting the amplitude of the reflection coefficient in all elements of the RIS. Since $\boldsymbol{\varphi}$ has constant magnitude inputs, (11) is a non-convex bounded optimization problem whose exact solution is not trivial to find.

3.2. Proposed Proximal Gradient Method

To address the optimization problem (11), we use the APG method as a heuristic approach in order to obtain a computationally efficient algorithm for computing the RIS matrix. Let us first rewrite (11) as

$$\min_{\boldsymbol{\varphi}} -\ln \det\left(\mathbf{I}_{Ns} + \frac{\rho}{P_n}\mathbf{F}^H\mathbf{H}^{Total^H}(\boldsymbol{\varphi})\mathbf{H}^{Total}(\boldsymbol{\varphi})\mathbf{F}\right) + \mathbf{I}_{|\boldsymbol{\varphi}|=a}(\boldsymbol{\varphi}) \tag{12}$$

where $\mathbf{I}_{|\boldsymbol{\varphi}=a|}(\boldsymbol{\varphi})$ is the set indicator function that returns zero if $|\boldsymbol{\varphi}| = a$ or $+\infty$ if not true. Based on the iterative APG approach described in [45], we compute the RIS angle vector at each iteration $(q + 1)$ as the solution of the following minimization problem

$$\boldsymbol{\varphi}^{(q+1)} = \min\left\{\mathbf{I}_{|\boldsymbol{\varphi}|=a}(\boldsymbol{\varphi}) + \frac{1}{2\mu}\|\mathbf{y}^{(q+1)} - \lambda^{(q)}\nabla f\left(\mathbf{y}^{(q+1)}\right) - \boldsymbol{\varphi}\|^2\right\} \tag{13}$$

where $\lambda^{(q)}$ is the step size, $f(\boldsymbol{\varphi})$ is the function defined as

$$f(\boldsymbol{\varphi}) = -\ln \det\left(\mathbf{I}_{Ns} + \frac{\rho}{P_N}\mathbf{F}^H\mathbf{H}^{Total^H}(\boldsymbol{\varphi})\mathbf{H}^{Total}(\boldsymbol{\varphi})\mathbf{F}\right) \tag{14}$$

and $\nabla f\left(\mathbf{y}^{(q+1)}\right)$ denotes the gradient of $f(.)$. It can be seen that this gradient is given by

$$\nabla f\left(\mathbf{y}^{(q+1)}\right) = -\text{diag}\left(\left(\mathbf{H}^{RIS,S}\right)^H\left[\mathbf{I}_{Nrx} + \mathbf{H}^{Total}\left(\mathbf{y}^{(q+1)}\right)\mathbf{F}\mathbf{F}^H\right.\right.$$
$$\left.\left.\mathbf{H}^{Total}\left(\mathbf{y}^{(q+1)}\right)^{-1} \times \mathbf{H}^{Total}\left(\mathbf{y}^{(q+1)}\right)\mathbf{F}\mathbf{F}^H\left(\mathbf{H}^{RIS,S}\right)^H\right)\right. \tag{15}$$

Regarding $\mathbf{y}^{(q+1)}$, it corresponds to a linear combination of the previous two points, $\boldsymbol{\varphi}^{(q)}$ and $\boldsymbol{\varphi}^{(q-1)}$, namely

$$\mathbf{y}^{(q+1)} = \boldsymbol{\varphi}^{(q)} + \boldsymbol{\omega}^{(q)}\left(\boldsymbol{\varphi}^{(q)} - \boldsymbol{\varphi}^{(q-1)}\right) \tag{16}$$

with $\boldsymbol{\omega}^{(q)}$ representing an extrapolation parameter that can be calculated as

$$\boldsymbol{\omega}^{(q)} = \frac{q}{q+3} \tag{17}$$

At this point, we can rewrite Equation (13) as

$$\boldsymbol{\varphi}^{(q+1)} = \text{prox}_{\mu\mathbf{I}(.)_{[.]=a}}\left(\mathbf{y}^{(q+1)} - \lambda^{(q)}\nabla f\left(\mathbf{y}^{(q+1)}\right)\right) \tag{18}$$

that is, we apply the proximal operator to $\boldsymbol{\varphi}^{(q+1)}$, which can be calculated as the projection on the set of vectors whose elements have modulus equal to a, resulting in

$$\boldsymbol{\varphi}^{(q+1)} = a\left(\mathbf{y}^{(q+1)} - \lambda^{(q)}\nabla f\left(\mathbf{y}^{(q+1)}\right)\right) \oslash \left[\mathbf{y}^{(q+1)} - \lambda^{(q)}\nabla f\left(\mathbf{y}^{(q+1)}\right)\right] \tag{19}$$

In this expression $\oslash$ corresponds to an element-by-element Hadamard division.

The step size, $\lambda^{(q)}$, that is required in (19) can be found by a line search procedure. In this paper we adopt the procedure proposed in [46]. Algorithm 1 summarizes all the steps of the proposed method. It is important to note that while we assumed a clustered channel model with LOS and NLOS components and with path loss modelled according to [35,42], recent works [40] are trying to define more accurate THz channel models, which may provide more insight on the achievable gains of THz systems. However, the proposed RIS optimization algorithm is not dependent on a specific channel model and can be directly applied to improved models that may arise in the future.

Algorithm 1 Accelerated Proximal Gradient (APG)

Input: $\boldsymbol{\varphi}^{(0)}$, $\lambda^{(0)}$
for $q = 0, \ldots Q$-1 **do**
  $\mathbf{y}^{(q+1)} = \boldsymbol{\varphi}^{(q)} + \boldsymbol{\omega}^{(q)}\left(\boldsymbol{\varphi}^{(q)} - \boldsymbol{\varphi}^{(q-1)}\right)$
  $\lambda = \lambda^{(q)}$
  Repeat
    $\boldsymbol{\psi} = a\left(\mathbf{y}^{(q+1)} - \lambda^{(q)}\nabla f\left(\mathbf{y}^{(q+1)}\right)\right) \oslash \left[\mathbf{y}^{(q+1)} - \lambda^{(q)}\nabla f\left(\mathbf{y}^{(q+1)}\right)\right]$
    $\hat{f}(\boldsymbol{\varphi}) = -\ln\det\left(\mathbf{I}_{Ns} + \mathbf{F}^H\mathbf{H}^{Total^H}\left(\mathbf{y}^{(q+1)}\right)\mathbf{H}^{Total}\left(\mathbf{y}^{(q+1)}\right)\mathbf{F}\right)$
      $+\mathbf{F}^H\left(\mathbf{y}^{(q+1)}\right)\left(\boldsymbol{\psi} - \mathbf{y}^{(q+1)}\right) + \frac{1}{2\lambda}\boldsymbol{\psi} - \mathbf{y}^{(q+1)^2}$
    if $f(\boldsymbol{\psi}) \leq \hat{f}(\boldsymbol{\psi})$
      break;
    Else
      $\lambda = \beta\lambda$(with $\beta \in]0,1[$)
    End
  End
  $\lambda^{(q+1)} = \lambda$
  $\boldsymbol{\varphi}^{(q+1)} = \boldsymbol{\psi}$
end for

3.3. Quantization

The proposed APG algorithm, as described previously, assumes continuous phase shifts in the phase-shifting diagonal matrix $\boldsymbol{\Phi}$. In practice, due to the hardware limitation in RIS-assisted systems [10], RIS elements can only support finite levels of phase shifts. Denoting N_b as the number of bits used in the quantization for the RIS, then the number of available phase levels is 2^{Nb}. For simplicity, we assume that the discrete phase shift values

are obtained by uniform interval quantization $[0, 2\pi]$. In this case the RIS optimization problem (11), must be modified as

$$\min_{\boldsymbol{\varphi}} -\ln \det\left(\mathbf{I}_{Ns} + \frac{\rho}{P_n}\mathbf{F}^H \mathbf{H}^{Total^H}(\boldsymbol{\varphi})\mathbf{H}^{Total}(\boldsymbol{\varphi})\mathbf{F}\right)$$

$$\text{subject to } \varphi_i \in \left\{a \cdot e^{\frac{2\pi}{2^{Nb}} i}\right\}, i = 0, \ldots, 2^{Nb} - 1 \tag{20}$$

The constraint in this problem still enforces the norm of the elements in the $\boldsymbol{\varphi}$ to remain one, but the possible phase shift values are limited to $\varphi_i \in \left\{a \cdot e^{\frac{2\pi}{2^{Nb}} i}\right\}, i = 0, \ldots, 2^{Nb} - 1$.

Algorithm 1 can be directly adapted to this new constraint by changing (19) to a projection of a given point onto a set of discrete phase shifts, which is equivalent to calculating the minimum distance between the point and all the set's possible values. However, we have verified numerically that Algorithm 1 performs better if we assume continuous phase shifts when computing the inner iterations, and the projection over the discrete phase shifts set is only computed in the end. Therefore, we adopt this configuration when considering quantization.

4. Numerical Results

In this section, we evaluate the achievable rate of the proposed RIS optimization algorithm with the aid of Monte Carlo simulations for different configurations. We consider a RIS-assisted UM-MIMO communication operating in an indoor environment, as in Figure 1. The coordinates of the BS, RIS, and user are (0 m, 0 m), ($\frac{\sqrt{2}}{2}$ m, $\frac{\sqrt{2}}{2}$ m), and (d, 1 m), respectively, where d is a value that varies along the simulations (changing the Tx-Rx distance). The transmit power at the BS is P_{tx} = 30 dBm and the noise power is $N_0 = -72.24$ dBm. The operating frequency of each RIS element is f = 300 GHz (i.e., $\lambda = 0.09$ cm), $k_{abs}(f) = 0.0033$, $d_s = d_r = \lambda/2 = 0.045$ cm, and the spacing between the RIS matrix elements is $d_{ris} = \lambda/2 = 0.045$ cm, resulting in $A_{RIS} = 0.045$ cm^2. Additionally, we consider a bandwidth of B = 10 GHz and assume a channel with $K_{Rice} = 10$ and $N_{ray} = 6$ NLOS paths. The antenna gains are $G_{tx} = G_{rx} = 22$ dBi. From Figures 2–5, a scenario with $N_s = 2$, $N_{tx} = 256$, and $N_{rx} = 4$, with a reflection coefficient amplitude of $a = 1$ for the RIS elements, was considered.

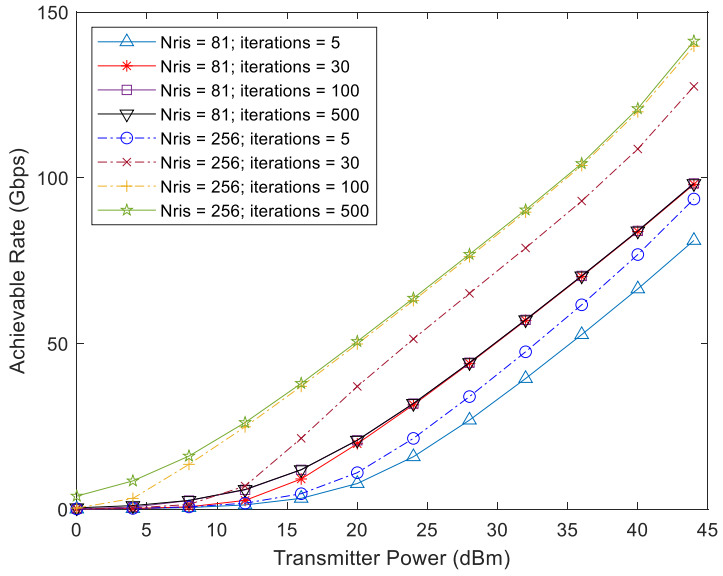

Figure 2. Achievable rate of the proposed APG versus power transmitted at the BS for different iteration values.

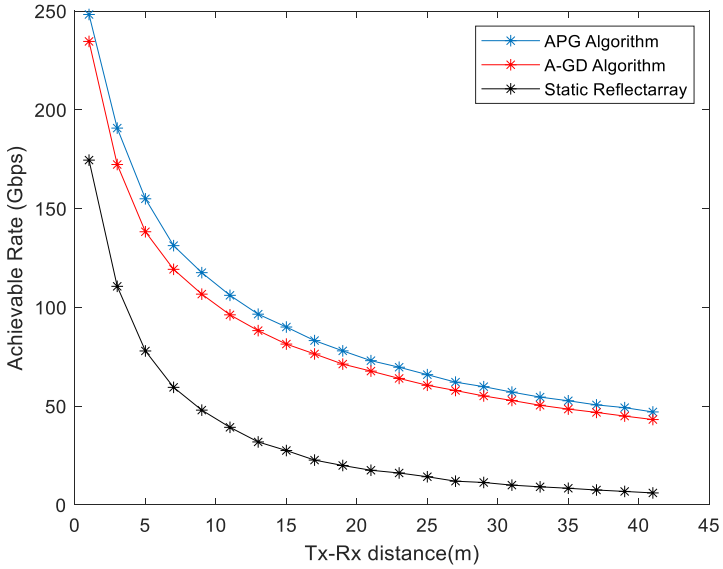

Figure 3. Achievable rate versus distance between BS–User for various schemes.

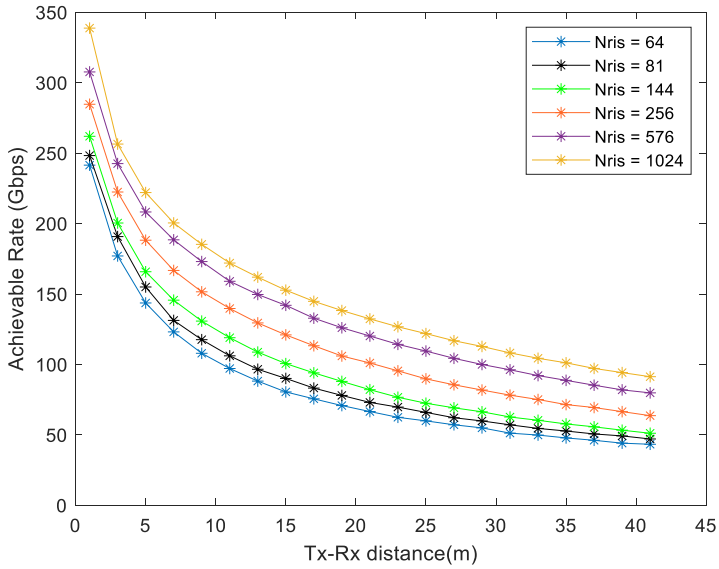

Figure 4. Achievable rate of the proposed APG for various elements in RIS versus distance between BS–User.

In order to better understand the behavior of the RIS optimization algorithm derived in Section 3, Figure 2 shows the achievable rate (in Gbps) versus the transmitted power (in dBm) with different values of iterations applied. In this particular case, the user is fixed at (0, 40 m). As expected, increasing the number of iterations allows the algorithm to find a better RIS solution. However, it can be seen that after around 100 iterations, the improvements become residual for both RIS sizes. Note that to avoid running unnecessary iterations, a simple stagnation condition that checks if the objective function, $f(\boldsymbol{\psi})$, decreased a minimum amount above a threshold, can be included to allow an early exit in the algorithm.

The following figures show the achievable rate (in Gbps) over the distance between the BS and the user (in meters). Figure 3 compares the proposed APG algorithm with a static reflectarray, and with the adaptive gradient descent (A-GD) algorithm from [27], considering a RIS with $N_{RIS} = 81$. Looking at the curves, we can observe that, as expected, the further away the user is from the BS, the lower the bitrate the system can achieve. From the results, we can conclude that the curve corresponding to a RIS acting as a simple reflector, achieves the worst results of the three. The other two curves, which consider

adaption of the individual RIS phases, clearly improve the results, with the proposed APG algorithm achieving higher rates than A-GD. The static reflectarray achieves rates above 100 Gbps to about 4 m, the A-GD about 10 m, and the APG about 12.5 m.

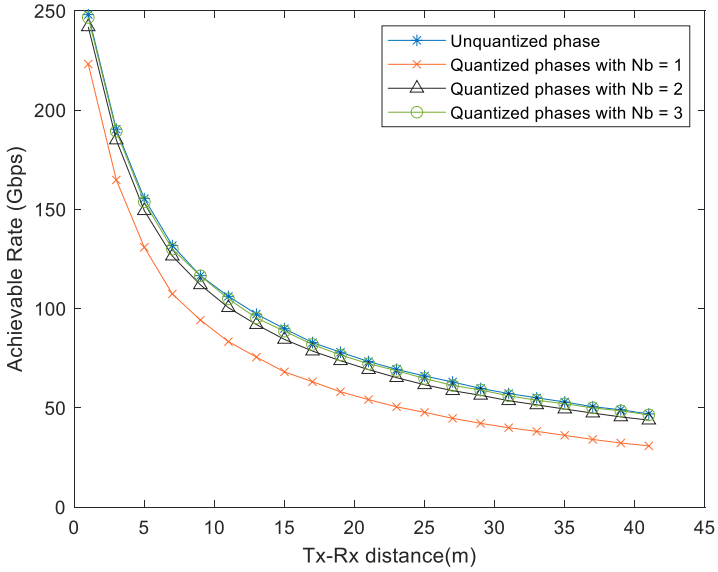

Figure 5. Achievable rate of the proposed APG for the case of discrete phase shifts versus distance between BS–User, considering N_{RIS} = 81.

For better assessment of the impact of the RIS on the achievable rate variation, we show in Figure 4 curves for increasing values of N_{RIS}. In this case, the physical size of the RIS is increasing, so it presents a larger reflection surface. We can observe that the achievable rate clearly improves for larger RIS. For example, when we increase N_{RIS} from 64 to 1024, we can observe an improvement of approximately 70 Gbps at 20m.

To further understand the behavior of the proposed APG method, it is necessary to consider the incidence of several non-idealities that are typical in an RIS-assisted communication system. The achievable rates for the cases of discrete phase shifts in an RIS and for the case of impact of imperfect channel knowledge are shown in Figures 5–7, respectively.

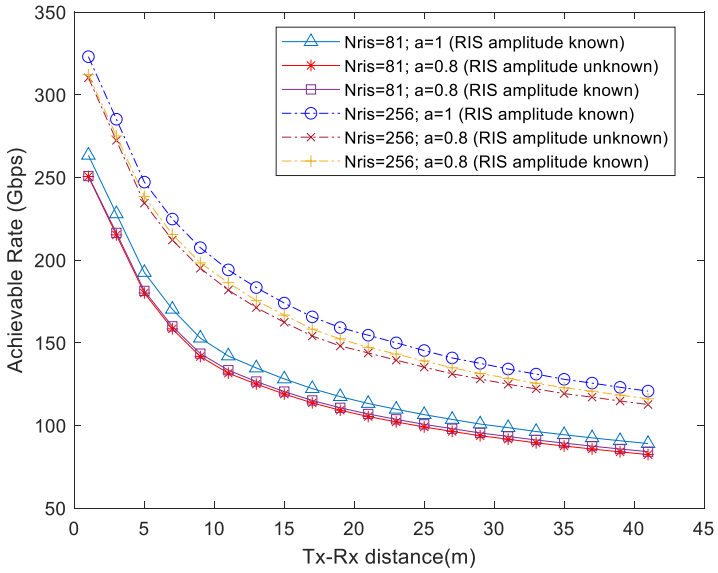

Figure 6. Achievable rate of the proposed APG versus distance between BS–User for the case of different values of RIS amplitudes.

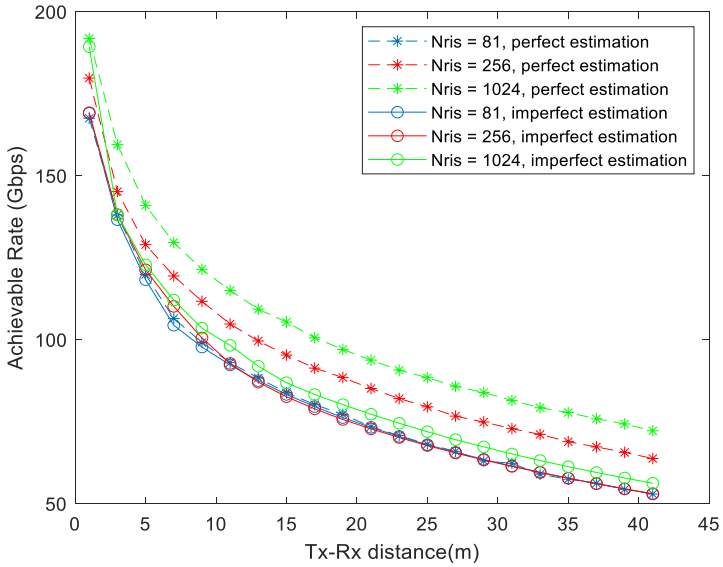

Figure 7. Achievable rate of the proposed APG for the case of perfect/imperfect estimation versus distance between BS–User, considering $N_s = 1$, $N_{tx} = 256$ and $N_{rx} = 4$.

From Figure 5, we conclude that the use of discrete 1-bit phase shifts can significantly penalize the achievable rate performance. For example, when the user is close to the BS and RIS, at 5 m distance, the rate decreases from 156 Gbps to 130 Gbps. However, using 2- or 3-bit phase shifters can be sufficient to achieve close-to-ideal performance with a reduction of only approximately 3 Gbps or 1 Gbps at 40 m, respectively. Thus, we conclude that the proposed algorithm is not very sensitive to quantization errors and a resolution of $N_b = 2$ should be enough to quantize the discrete phase shifts of the RIS elements without a substantial performance degradation.

Even though in the previous simulations we were assuming ideal phase shifters (reflection coefficients having unitary amplitude, $a = 1$) at the RIS elements, in realistic scenarios, this amplitude will be smaller as there will be some loss [27]. Therefore, Figure 6 compares the effect of a lower reflection coefficient amplitude (the value a = 0.8 was selected based on [47]) as well as the impact of not knowing the correct reflection amplitude in the RIS optimization algorithm. As would be expected, the achievable rate decreases slightly when the value of the amplitude of the reflection coefficient of the RIS elements is lower than one regardless of the value of N_{RIS}. When the RIS elements have loss and the algorithm does not know the exact value of the reflection amplitude, which in the figure corresponds to having phase shifters with $a = 0.8$ while the algorithm assumes that $a = 1$, it can be seen that the additional degradation is relatively small. For example, when the user is located 10 m away from the BS, the rate decreases only from 133 Gbps to 131 Gbps and from 186 Gbps to 181 Gbps, with $N_{RIS} = 81$ and $N_{RIS} = 256$, respectively.

In Figure 7, we evaluate the impact of imperfect channel knowledge for a scenario where $N_s = 1$, $N_{tx} = 256$, and $N_{rx} = 4$. In this case, we include curves that consider knowledge of only the LoS component, i.e., $\hat{\mathbf{H}} = \mathbf{H}_{LOS}$. Observing the results, we can see that, as expected, the optimal achievable rate decreases with imperfect channel knowledge, independently of the $N_{RIS.}$ However, the higher the N_{RIS}, the sharper is the reduction level. For example, at 40 m distance with $N_{RIS} = 81$ the rate decreased from 53 Gbps to 52 Gbps, whereas with $N_{RIS} = 256$ it decreased from 63 Gbps to 53 Gbps, and with $N_{RIS} = 1024$ it reduced from 73 Gbps to 56 Gbps.

5. Conclusions

In this paper, we studied a UM-MIMO system operating in the THz band where a base station transmits to a user with the aid of an RIS. In order to compute the individual phase shifts of the RIS elements and, at the same time, cope with the large problem setting

that is typical in RIS-aided UM-MIMO systems, we proposed the use of a low complexity accelerated proximal gradient algorithm that attempts to maximize the achievable rate. Numerical results confirm the effectiveness of the proposed approach, which is able to support large transmission rates for extended distances, even without a direct link between the transmitter and receiver. In fact, it was observed that the algorithm improves the range between 30% and 120% when compared to other existing approaches, for a reference rate of 100 Gbps with only 81 RIS elements. As the number of RIS elements increased from $N_{ris} = 64$ to $N_{ris} = 1024$, it was possible to achieve an improvement on the achievable rate near 60%. Furthermore, it was also shown that practical low resolution RIS elements may suffice to achieve close to unquantized performance. Additionally, it was observed that the achievable rate decreased slightly if the value of the amplitude of the reflection coefficient of the RIS elements was lower than one, regardless of the value of N_{RIS}. However, the lack of accurate knowledge about the value of this amplitude caused degradations of only 1.5–3.8%, which means the algorithm is not very sensitive to this aspect.

While the numerical performance analysis presented in this paper is important in order to capture the potential achievable gains of UM-MIMO THz systems, these gains should be validated via experimental testbeds as soon as adequate devices become available, which should be possible in the near future. Furthermore, three main directions can be followed as future work in order to extend the proposed approach. The first should consider the design of the system with more than one RIS panel, as it would correspond to a more useful scenario that could guarantee more coverage in the area around the BS and also increase the number of potential LOS links. The second is to extend the system to multiuser scenarios where the BS and the RIS have to be configured in order to establish multiple simultaneous links with different users. Finally, the last aspect concerns the study of low latency channel estimation schemes suitable for the THz RIS and incorporate the potential error in the RIS optimization in order to obtain a more robust design.

Author Contributions: Conceptualization, J.P., N.S. and M.R.; methodology, J.P. and N.S.; software, J.P. and N.S.; validation, J.P., J.P.P. and N.S.; formal analysis, J.P. and N.S.; investigation, J.P., J.P.P. and N.S.; resources, J.P.P., N.S. and M.R.; data curation, J.P.; writing—original draft preparation, J.P., J.P.P., N.S. and M.R.; writing—review and editing, J.P., J.P.P., N.S. and M.R.; visualization, J.P.; supervision, N.S. and M.R.; project administration, N.S. and M.R.; funding acquisition, N.S. and M.R. All authors have read and agreed to the published version of the manuscript.

Funding: This work was supported by the FCT—Fundação para a Ciência e Tecnologia under the grant 2020.05621.BD. The authors also acknowledge the funding provided by FCT/MCTES through national funds and, when applicable, co-funded EU funds under the project UIDB/50008/2020.

Conflicts of Interest: The authors declare no conflict of interest.

References

1. Dang, S.; Amin, O.; Shihada, B.; Alouini, M. What should 6G be? *Nat. Electron.* **2020**, *3*, 20–29. [CrossRef]
2. Saad, W.; Bennis, M.; Chen, M. A Vision of 6G Wireless Systems: Applications, Trends, Technologies, and Open Research Problems. *IEEE Netw.* **2020**, *34*, 134–142. [CrossRef]
3. Rajatheva, N.; Atzeni, I.; Bjornson, E.; Bourdoux, A.; Buzzi, S.; Dore, J.B.; Erkucuk, S.; Fuentes, M.; Guan, K.; Hu, Y. White paper on broadband connectivity in 6G. *arXiv* **2020**, arXiv:2004.14247.
4. Alibakhshikenari, M.; Virdee, B.S.; Shukla, P.; See, C.H.; Abd-Alhameed, R.A.; Falcone, F.; Quazzane, K.; Limiti, E. Isolation enhancement of densely packed array antennas with periodic MTM-photonic bandgap for SAR and MIMO systems. *IET Microw. Antennas Propag.* **2020**, *14*, 183–188. [CrossRef]
5. Althuwayb, A. Enhanced radiation gain and efficiency of a metamaterial-inspired wideband microstrip antenna using substrate integrated waveguide technology for sub-6 GHz wireless communication systems. *Microw. Opt. Technol. Lett.* **2021**, *63*, 1892–1898. [CrossRef]
6. Sarieddeen, H.; Alouini, M.; Al-Naffouri, T. An Overview of Signal Processing Techniques for Terahertz Communications. *arXiv* **2020**, arXiv:2005.13176v2. [CrossRef]
7. Han, C.; Wu, Y.; Chen, Z.; Wang, X. Terahertz communications (TeraCom): Challenges and impact on 6G wireless systems. *arXiv* **2019**, arXiv:1912.06040.
8. Elayan, H.; Amin, O.; Shihada, B.; Shubair, R.; Alouini, M. Terahertz Band: The Last Piece of RF Spectrum Puzzle for Communication Systems. *IEEE Open J. Commun. Soc.* **2020**, *1*, 1–32. [CrossRef]

9. O'Hara, J.; Ekin, S.; Choi, W.; Song, I. A Perspective on Terahertz Next-Generation Wireless Communications. *Technologies* **2019**, *7*, 43. [CrossRef]
10. Wu, Q.; Zhang, R. Towards Smart and Reconfigurable Environment: Intelligent Reflecting Surface Aided Wireless Network. *IEEE Commun. Mag.* **2019**, *58*, 106–112. [CrossRef]
11. Di Renzo, M.; Debbah, M.; Phan-Huy, D.; Zappone, A.; Alouini, M.; Yuen, C.; Sciancalepore, V.; Alexandropoulos, G.; Hoydis, J.; Gacanin, H.; et al. Smart radio environments empowered by reconfigurable AI meta-surfaces: An idea whose time has come. *EURASIP J. Wirel. Commun. Netw.* **2019**, *2019*, 129. [CrossRef]
12. Chen, Z.; Ma, X.; Han, C.; Wen, Q. Towards intelligent reflecting surface empowered 6G terahertz communications: A survey. *China Commun.* **2021**, *18*, 93–119. [CrossRef]
13. Wu, Q.; Zhang, R. Beamforming Optimization for Wireless Network Aided by Intelligent Reflecting Surface with Discrete Phase Shifts. *IEEE Trans. Commun.* **2020**, *68*, 1838–1851. [CrossRef]
14. Dai, L.; Wang, B.; Wang, M.; Yang, X.; Tan, J.; Bi, S.; Xu, S.; Yang, F.; Chen, Z.; Renzo, M.; et al. Reconfigurable Intelligent Surface-Based Wireless Communications: Antenna Design, Prototyping, and Experimental Results. *IEEE Access* **2020**, *8*, 45913–45923. [CrossRef]
15. Gong, S.; Lu, X.; Hoang, D.T.; Niyato, D.; Shu, L.; Kim, D.I.; Liang, Y.-C. Toward Smart Wireless Communications via Intelligent Reflecting Surfaces: A Contemporary Survey. *IEEE Commun. Surv. Tutor.* **2020**, *22*, 2283–2314. [CrossRef]
16. Sarieddeen, H.; Saeed, N.; Al-Naffouri, T.; Alouini, M. Next Generation Terahertz Communications: A Rendezvous of Sensing, Imaging, and Localization. *IEEE Commun. Mag.* **2020**, *58*, 69–75. [CrossRef]
17. Akyildiz, I.; Han, C.; Nie, S. Combating the Distance Problem in the Millimeter Wave and Terahertz Frequency Bands. *IEEE Commun. Mag.* **2018**, *56*, 102–108. [CrossRef]
18. Yongzhi, W.; Chong, H. Interference and Coverage Analysis for Indoor Terahertz Wireless Local Area Networks. In *IEEE Globecom Workshops (GC Wkshps)*; IEEE: Piscataway, NJ, USA, 2019; pp. 1–6.
19. Kürner, T.; Priebe, S. Towards THz Communications—Status in Research, Standardization and Regulation. *J. Infrared Millim. Terahertz Waves* **2013**, *35*, 53–62. [CrossRef]
20. Petrov, V.; Pyattaev, A.; Moltchanov, D.; Koucheryavy, Y. Terahertz band communications: Applications, research challenges, and standardization activities. In Proceedings of the 8th International Congress on Ultra Modern Telecommunications and Control Systems and Workshops (ICUMT), Lisbon, Portugal, 18–20 October 2016; pp. 183–190.
21. Alghamdi, R.; Alhadrami, R.; Alhothali, D.; Almorad, H.; Faisal, A.; Helal, S.; Shalabi, R.; Asfour, R.; Hammad, N.; Shams, A.; et al. Intelligent Surfaces for 6G Wireless Networks: A Survey of Optimization and Performance Analysis Techniques. *IEEE Access* **2020**, *8*, 202795–202818. [CrossRef]
22. Perovic, N.; Tran, L.; Di Renzo, M.; Flanagan, M. Achievable Rate Optimization for MIMO Systems with Reconfigurable Intelligent Surfaces. *IEEE Trans. Wirel. Commun.* **2021**, *20*, 3865–3882. [CrossRef]
23. Hou, T.; Liu, Y.; Song, Z.; Sun, X.; Chen, Y.; Hanzo, L. MIMO Assisted Networks Relying on Intelligent Reflective Surfaces. *arXiv* **2019**, arXiv:1910.00959.
24. Zhang, J.; Liu, J.; Ma, S.; Wen, C.; Jin, S. Large System Achievable Rate Analysis of RIS-Assisted MIMO Wireless Communication with Statistical CSIT. *IEEE Trans. Wirel. Commun.* **2021**, *20*, 5572–5585. [CrossRef]
25. Wu, Q.; Zhang, R. Intelligent Reflecting Surface Enhanced Wireless Network via Joint Active and Passive Beamforming. *IEEE Trans. Wirel. Commun.* **2019**, *18*, 5394–5409. [CrossRef]
26. Di, B.; Zhang, H.; Song, L.; Li, Y.; Han, Z.; Poor, H. Hybrid Beamforming for Reconfigurable Intelligent Surface based Multi-User Communications: Achievable Rates with Limited Discrete Phase Shifts. *IEEE J. Sel. Areas Commun.* **2020**, *38*, 1809–1822. [CrossRef]
27. Ma, X.; Chen, Z.; Yan, L.; Han, C.; Wen, Q. Joint Hardware Design and Capacity Analysis for Intelligent Reflecting Surface Enabled Terahertz MIMO Communications. *arXiv* **2020**, arXiv:2012.06993v2.
28. Nie, S.; Akyildiz, I. Beamforming in Intelligent Environments based on Ultra-Massive MIMO Platforms in Millimeter Wave and Terahertz Bands. In Proceedings of the IEEE International Conference on Acoustics, Speech and Signal Processing—Proceedings, ICASSP, Barcelona, Spain, 4–8 May 2020; pp. 8683–8687.
29. Han, C.; Yan, L.; Yuan, J. Hybrid Beamforming for Terahertz Wireless Communications: Challenges, Architectures, and Open Problems. *IEEE Wirel. Commun.* **2021**, *28*, 198–204. [CrossRef]
30. Ning, B.; Tian, Z.; Chen, Z.; Han, C.; Yuan, J.; Li, S. Prospective Beamforming Technologies for Ultra-Massive MIMO in Terahertz Communications: A Tutorial. *arXiv* **2021**, arXiv:2107.03032.
31. Akyildiz, I.; Jornet, J. Realizing Ultra-Massive MIMO (1024 × 1024) communication in the (0.06–10) Terahertz band. *Nano Commun. Netw.* **2016**, *8*, 46–54. [CrossRef]
32. Singh, A.; Andrello, M.; Thawdar, N.; Jornet, J. Design and Operation of a Graphene-Based Plasmonic Nano-Antenna Array for Communication in the Terahertz Band. *IEEE J. Sel. Areas Commun.* **2020**, *38*, 2104–2117. [CrossRef]
33. Thawdar, N.; Andrello, M.; Jornet, J. Modeling and Performance Analysis of a Reconfigurable Plasmonic Nano-Antenna Array Architecture for Terahertz Communications. In Proceedings of the 5th ACM International Conference on Nanoscale Computing and Communication, Reykjavik, Iceland, 5–7 September 2018; Volume 18, pp. 1–6.
34. Andrello, M.; Singh, A.; Thawdar, N.; Jornet, J. Dynamic Beamforming Algorithms for Ultra-directional Terahertz Communication Systems Based on Graphene-based Plasmonic Nano-antenna Arrays. In Proceedings of the Conference Record—Asilomar Conference on Signals, Systems, and Computers, Pacific Grove, CA, USA, 28–31 October 2018; pp. 1558–1563.

35. Dovelos, K.; Assimonis, S.; Ngo, H.; Bellalta, B.; Matthaiou, M. Intelligent Reflecting Surfaces at Terahertz Bands: Channel Modeling and Analysis. In Proceedings of the 2021 IEEE International Conference on Communications Workshops, ICC Workshops 2021—Proceedings, Montreal, QC, Canada, 14–23 June 2021.
36. Akyildiz, I.; Jornet, J.; Han, C. TeraNets: Ultra-broadband communication networks in the terahertz band. *IEEE Wirel. Commun.* **2014**, *21*, 130–135. [CrossRef]
37. Smari, B.; Labidi, M.; Choubani, F. Mutual coupling reduction in metamaterial antenna for terahertz application. *Appl. Phys. A Mater. Sci. Process.* **2019**, *125*, 695. [CrossRef]
38. Zakrajsek, L.; Einarsson, E.; Thawdar, N.; Medley, M.; Jornet, J. Design of graphene-based plasmonic nano-antenna arrays in the presence of mutual coupling. In Proceedings of the 2017 11th European Conference on Antennas and Propagation (EUCAP), Paris, France, 19–24 March 2017; pp. 1381–1385.
39. Zhang, B.; Jornet, J.; Akyildiz, I.; Wu, Z. Mutual Coupling Reduction for Ultra-Dense Multi-Band Plasmonic Nano-Antenna Arrays Using Graphene-Based Frequency Selective Surface. *IEEE Access* **2019**, *7*, 33214–33225. [CrossRef]
40. Tarboush, S.; Sarieddeen, H.; Chen, H.; Loukil, M.H.; Jemaa, H.; Alouini, M.-S.; Al-Naffouri, T.Y. TeraMIMO: A Channel Simulator for Wideband Ultra-Massive MIMO Terahertz Communications. *arXiv* **2021**, arXiv:2104.11054v3. [CrossRef]
41. Saleh, A.; Valenzuela, R. A Statistical Model for Indoor Multipath Propagation. *IEEE J. Sel. Areas Commun.* **1987**, *5*, 128–137. [CrossRef]
42. Tang, W.; Chen, X.; Chen, M.Z.; Dai, J.Y.; Han, Y.; Di Renzo, M.; Jin, S.; Cheng, Q.; Cui, T.J. Path Loss Modeling and Measurements for Reconfigurable Intelligent Surfaces in the Millimeter-Wave Frequency Band. *arXiv* **2021**, arXiv:2101.08607v1.
43. Yu, X.; Zhang, J.; Letaief, B. Doubling Phase Shifters for Efficient Hybrid Precoder Design in Millimeter-Wave Communication Systems. *J. Commun. Inf. Netw.* **2019**, *4*, 51–67.
44. Pavia, J.P.; Velez, V.; Ferreira, R.; Souto, N.; Ribeiro, M.; Silva, J.; Dinis, R. Low Complexity Hybrid Precoding Designs for Multiuser mmWave/THz Ultra Massive MIMO Systems. *Sensors* **2021**, *21*, 6054. [CrossRef]
45. Parikh, N. Proximal algorithms. *Found. Trends Optim.* **2014**, *1*, 123–231.
46. Beck, A.; Teboulle, M. Gradient-based algorithms with applications to signal recovery problems. In *Convex Optimization in Signal Processing and Communications*; Palomar, D., Eldar, Y., Eds.; Convex Optimization in Signal Processing and Communications; Cambridge University Press: Cambridge, UK, 2010; pp. 42–88.
47. Ning, B.; Chen, Z.; Chen, W.; Du, Y.; Fang, J. Terahertz Multi-User Massive MIMO with Intelligent Reflecting Surface: Beam Training and Hybrid Beamforming. *IEEE Trans. Veh. Technol.* **2021**, *70*, 1376–1393. [CrossRef]